Robust Control of Solid Oxide Fuel Cell Ultra-Capacitor Hybrid System

Tahar Allag
Graduate Student

Tuhin Das
Assistant Professor

Rochester Institute of Technology
Mechanical Engineering Department
Rochester, NY 14623
E-mail: tkdeme@rit.edu

Abstract

Mitigating fuel starvation and improving load-following capability of solid oxide fuel cells (SOFC) are conflicting control objectives. In this paper we address this issue using a hybrid SOFC ultra-capacitor configuration. Fuel starvation is prevented by regulating the fuel cell current using a steady-state invariant relationship involving fuel utilization, fuel flow and current. Two comprehensive control strategies are developed. The first is a Lyapunov-based nonlinear control and the second is a standard H_∞ robust control. Both strategies additionally control the state of charge (SOC) of the ultra-capacitor that provides transient power compensation. A hardware-in-the-loop test-stand is developed where the proposed control strategies are verified.

©2011 IEEE. Personal use of this material is permitted. Permission from IEEE must be obtained for all other uses, in any current or future media, including reprinting/republishing this material for advertising or promotional purposes, creating new collective works, for resale or redistribution to servers or lists, or reuse of any copyrighted component of this work in other works.

1 INTRODUCTION

Among different fuel cell technologies, SOFC technology has attracted significant interest in recent years. SOFCs are solid state devices that are fuel flexible, tolerant to impurities and operate at high temperatures ($800° - 1000°$C). The high temperatures allow internal reforming, promote rapid reaction kinetics with non-precious metals and produce high quality by-product heat for co-generation or for use in a bottoming cycle, [1, 2].

In spite of these attributes, application of SOFCs has been limited due to their poor load following capability [3], and has particularly precluded their use in applications involving rapid power variations. This is a common drawback of fuel cells. It is attributed to the slow dynamic response of the fuel and air delivery systems consisting of valves, pumps and reformers, [4, 5, 6, 7]. It is manifested as hydrogen or oxygen starvation and drastic voltage drop when the fuel cell is directly exposed to rapid power transients. The phenomenon adversely affects cell durability through anode oxidation [7] and reversal of cell potential, leading to catalyst corrosion [8]. Multiple authors have addressed this issue by augmenting the fuel cell with an electrical storage device. In [4], the authors develop a current control strategy to minimize the fuel cell's voltage droop. In [5], fuel cell current is rate limited to prevent starvation in a fuel cell ultra-capacitor hybrid. In [9], the authors propose a robust load governor for preventing oxygen starvation. In [6], a Model Predictive Control (MPC) is developed for a fuel cell ultra-capacitor system that minimizes oxygen starvation, bounds the ultra-capacitor's state-of-charge (SOC), and prevents compressor surge and choke. An MPC based approach for improving battery performance and avoiding fuel cell and battery degradation is used in [10].

In addition, a number of papers have proposed control of hybrid fuel cells without specifically addressing the above mentioned constraints, but providing a rich spectrum of control approaches. In [11, 12, 13], rule-based control strategies are developed where the hybrid system switches between discrete operating modes. In [14], the proposed control strategy regulates the fuel cell current based on the battery SOC. In [15], a two-loop control strategy

is proposed for a hybrid fuel cell where an inner loop regulates the DC bus voltage and an outer loop regulates the fuel cell current. In [16], a sliding-mode control [17] is developed for a fuel cell hybrid system. In [18], the authors develop a differential flatness [19] based control for a fuel cell ultra-capacitor system. In [20], optimal power distribution is obtained in a hybrid fuel cell vehicle by local minimization of an equivalent fuel consumption variable.

A majority of the work mentioned above pertain to PEMFCs. Control development for hybrid SOFCs systems are in preliminary stages. For SOFCs, the load-following limitations of the fuel cell are reflected in the transient response of a performance variable, namely fuel utilization. Fuel utilization U is defined as the ratio of hydrogen consumption to the net available hydrogen in the anode. In the formulation of U, not only is the available hydrogen considered but the hydrogen that can be generated from other species through internal reforming are also accounted for [21]. This is because of SOFC's tolerance to impurities that allows the reformer exhaust gas-mixture to be directly sent to the anode with minimal or no purification. While high utilization implies high efficiency, very high utilization leads to reduced partial pressure of hydrogen in the anode, leading to voltage drop and anode oxidation [7]. Low fuel utilization on the other hand results in under-used fuel, [22]. Typically, $80 - 90\%$ is set as the target range for maximizing the cell's electric efficiency, [21, 22, 23].

Control of U around a target value has been adopted in a number of studies [24, 25, 26, 27]. However, measurement of U requires several species-specific concentration sensors that are avoided due to cost and reliability considerations. Observer designs are possible [28, 29, 30, 31], however they can be computation intensive, and rely on accurate mathematical models. In contrast, in this paper we propose control of U by combining an *invariant relationship* of the SOFC system [32], with a current regulation strategy. The approach achieves a target steady-state U and attenuates transient departure from this target. The deficit or surplus power delivered by the SOFC due to current regulation is compensated by an ultra-capacitor. Current regulation is incorporated within a robust control scheme that additionally controls the ultra-capacitor's SOC. The control objectives are satisfied in

presence of uncertainties. Two control strategies are developed, a nonlinear control and an H_∞ control. This work addresses hydrogen starvation but oxygen starvation is not considered as it is seldom observed in typical SOFC systems. This is because in the absence of coolants, excess air (air utilization $\approx 20 - 25\%$, [33]) is used for temperature control [7].

SOFC systems are in developmental stages and their commercial availability is extremely limited. Also, the costs and necessary infrastructural support for experimentation with prototypes are prohibitive. Hence, for control verification we use a control-oriented mathematical model of a tubular SOFC system developed in our prior research, presented in [32, 34]. The model captures the thermodynamics, chemical kinetics, heat transfer and pressure dynamics phenomena and has been validated against results in [7] and [33]. We develop an experimental test-stand where the SOFC system is emulated by combining a real-time implementation of the model with a programmable power supply. The emulated SOFC is integrated with commercially available power electronics components and an ultra-capacitor.

The paper is organized as follows: A system description and open-loop results are presented in section 2. The invariant relationship is derived and used for open-loop control in section 3. The current regulation method is presented in section 4, followed by a discussion in section 5 on system-induced flow delays. The hybrid fuel cell configuration and the control designs are presented in sections 6 and 7. The experimental test-stand is explained in section 8, followed by results in section 9. Finally concluding remarks and acknowledgments are stated in sections 10 and 11, and references are listed.

2 FUEL CELL SYSTEM

We consider a steam reformer based tubular SOFC system. The system consists of three primary components, namely, the steam reformer, the fuel cell stack and the combustor. Methane is chosen as the fuel for the system, with a molar flow rate of $\dot{N}_f$. The analysis and control approach presented in this paper can be extended to other fuels and system

configurations. The system is presented in Fig.1.

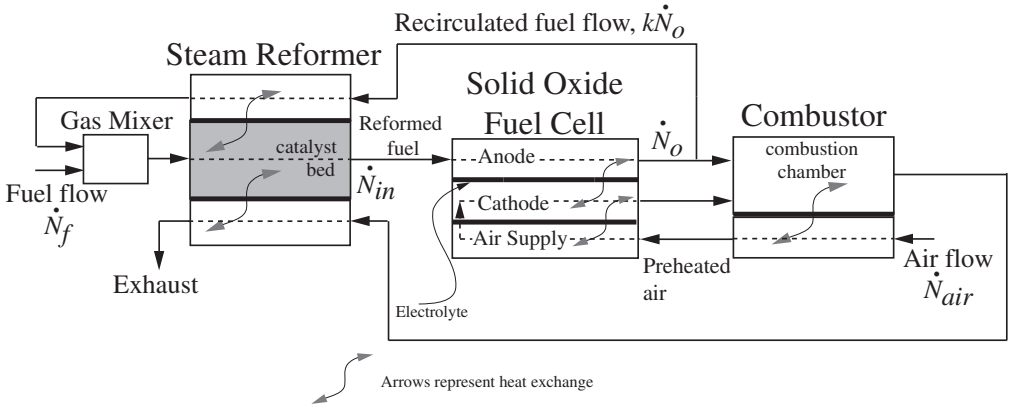

Figure 1: Schematic Diagram of SOFC System

The reformer produces a hydrogen-rich gas which is supplied to the anode of the fuel cell. Electrochemical reactions occurring at the anode due to current draw results in a steam-rich gas mixture at its exit. A known fraction k of the anode exhaust is recirculated through the reformer into a mixing chamber where fuel is added. The mixing of the two fluid streams and pressurization is achieved in the gas mixer using an ejector or a recirculating fuel pump, [35]. The steam reforming process occurring in the reformer catalyst bed is an endothermic process. The energy required to sustain the process is supplied from two sources, namely, the combustor exhaust that is passed through the reformer, and the aforementioned recirculated anode flow, as shown in Fig.1. The remaining anode exhaust is mixed with the cathode exhaust in the combustion chamber. The combustor also serves to preheat the cathode air which has a molar flow rate of $\dot{N}_{air}$. The tubular construction of each cell causes the air to first enter the cell through the air supply tube and then reverse its direction to enter the cathode chamber. For steam reforming of methane we consider a packed-bed tubular reformer with nickel-alumina catalyst. The three main reactions in steam reforming of methane are, [36]:

$$\begin{aligned} &\text{(I)} \quad CH_4 + H_2O \leftrightarrow CO + 3H_2 \qquad \text{(II)} \quad CO + H_2O \leftrightarrow CO_2 + H_2 \\ &\text{(III)} \quad CH_4 + 2H_2O \leftrightarrow CO_2 + 4H_2 \end{aligned} \tag{1}$$

Internal reforming reactions I, II and III in Eq.(1) occur in the anode due to high tempera-

tures and the presence of nickel catalyst. The primary electrochemical process is

$$\text{(IV)} \quad H_2 + O^{2-} \rightarrow H_2O + 2e \tag{2}$$

Simultaneous electrochemical conversion of CO to CO_2 is ignored since its rate is much slower in presence of reactions II and IV, [37]. Details of the system model are presented in [34]. Fuel utilization U is mathematically defined as, [7, 21, 23]:

$$U \triangleq 1 - \frac{\dot{N}_o \left(4\mathcal{X}_{1,a} + \mathcal{X}_{2,a} + \mathcal{X}_{4,a}\right)}{\dot{N}_{in} \left(4\mathcal{X}_{1,r} + \mathcal{X}_{2,r} + \mathcal{X}_{4,r}\right)} \tag{3}$$

where, $\mathcal{X}_{1,a}$, $\mathcal{X}_{2,a}$, $\mathcal{X}_{4,a}$ and $\mathcal{X}_{1,r}$, $\mathcal{X}_{2,r}$, $\mathcal{X}_{4,r}$ are the molar concentrations of CH_4, CO and H_2 in the anode and the reformer respectively and $\dot{N}_o$ and $\dot{N}_{in}$ are shown in Fig.1. Eq.(3) is based on the observation that a CH_4 and a CO molecule can yield at most four molecules and one molecule of H_2 respectively, as indicated by reactions I, II and III in Eq.(2).

3 OPEN-LOOP CONTROL OF U

The molar balance equations of individual species in the reformer and anode are:

$$\begin{aligned}
\dot{N}_r\mathcal{X}_{1,r} + N_r\dot{\mathcal{X}}_{1,r} &= k\dot{N}_o\mathcal{X}_{1,a} - \dot{N}_{in}\mathcal{X}_{1,r} + \mathcal{R}_{1,r} + \dot{N}_f \\
\dot{N}_r\mathcal{X}_{2,r} + N_r\dot{\mathcal{X}}_{2,r} &= k\dot{N}_o\mathcal{X}_{2,a} - \dot{N}_{in}\mathcal{X}_{2,r} + \mathcal{R}_{2,r} \\
\dot{N}_r\mathcal{X}_{3,r} + N_r\dot{\mathcal{X}}_{3,r} &= k\dot{N}_o\mathcal{X}_{3,a} - \dot{N}_{in}\mathcal{X}_{3,r} - \mathcal{R}_{1,r} - \mathcal{R}_{2,r} \\
\dot{N}_r\mathcal{X}_{4,r} + N_r\dot{\mathcal{X}}_{4,r} &= k\dot{N}_o\mathcal{X}_{4,a} - \dot{N}_{in}\mathcal{X}_{4,r} - 4\mathcal{R}_{1,r} - \mathcal{R}_{2,r} \\
\dot{N}_r\mathcal{X}_{5,r} + N_r\dot{\mathcal{X}}_{5,r} &= k\dot{N}_o\mathcal{X}_{5,a} - \dot{N}_{in}\mathcal{X}_{5,r} + 2\mathcal{R}_{1,r} + \mathcal{R}_{2,r}
\end{aligned} \tag{4}$$

$$\begin{aligned}
\dot{N}_a\mathcal{X}_{1,a} + N_a\dot{\mathcal{X}}_{1,a} &= \dot{N}_{in}\mathcal{X}_{1,r} - \dot{N}_o\mathcal{X}_{1,a} + \mathcal{R}_{1,a} \\
\dot{N}_a\mathcal{X}_{2,a} + N_a\dot{\mathcal{X}}_{2,a} &= \dot{N}_{in}\mathcal{X}_{2,r} - \dot{N}_o\mathcal{X}_{2,a} + \mathcal{R}_{2,a} \\
\dot{N}_a\mathcal{X}_{3,a} + N_a\dot{\mathcal{X}}_{3,a} &= \dot{N}_{in}\mathcal{X}_{3,r} - \dot{N}_o\mathcal{X}_{3,a} - \mathcal{R}_{1,a} - \mathcal{R}_{2,a} \\
\dot{N}_a\mathcal{X}_{4,a} + N_a\dot{\mathcal{X}}_{4,a} &= \dot{N}_{in}\mathcal{X}_{4,r} - \dot{N}_o\mathcal{X}_{4,a} - 4\mathcal{R}_{1,a} - \mathcal{R}_{2,a} - r_e \\
\dot{N}_a\mathcal{X}_{5,a} + N_a\dot{\mathcal{X}}_{5,a} &= \dot{N}_{in}\mathcal{X}_{5,r} - \dot{N}_o\mathcal{X}_{5,a} + 2\mathcal{R}_{1,a} + \mathcal{R}_{2,a} + r_e
\end{aligned} \tag{5}$$

$$r_e = i_{fc}\mathcal{N}_{cell}/nF \tag{6}$$

where, r_e is the rate of electrochemical reaction. In Eqs.(4) and (5), $\mathcal{X}_{i,r}$ and $\mathcal{X}_{i,a}$ are the molar concentrations of species in the reformer and anode respectively, with $i = 1, 2, \cdots, 5$ representing CH_4, CO, CO_2, H_2 and H_2O in that order. N_r and N_a are the molar contents of the reformer and the anode, and k is the constant and known recirculation fraction shown in Fig.1. $\mathcal{R}_{1,r}$, $\mathcal{R}_{2,r}$ and $\mathcal{R}_{1,a}$, $\mathcal{R}_{2,a}$ are the rates of formation of CH_4 and CO in the reformer and anode respectively. In Eq.(6), i_{fc} is the fuel cell current, $\mathcal{N}_{cell}$ is number of series-connected cells, $n = 2$ is the number of electrons participating in an electrochemical reaction, and $F = 96485.34$Coul./mole is the Faraday's constant. Further details about the equations can be found in [32, 34]. From Eqs.(3), (4), (5) and (6), noting that the left hand sides of Eqs.(4) and (5) are zero at steady-state, the steady-state utilization U_{ss} is obtained as

$$U_{ss} = (1-k)/\left[\left(4nF\dot{N}_f/i_{fc}\mathcal{N}_{cell}\right) - k\right] \tag{7}$$

Note that Eq.(7) is independent of the reaction rates $\mathcal{R}_{1,r}$, $\mathcal{R}_{2,r}$, $\mathcal{R}_{1,a}$ $\mathcal{R}_{2,a}$ and the flow rates $\dot{N}_{in}$, $\dot{N}_o$. Equation (7) is valid in steady-state and is invariant with respect to variations in operating temperature, operating pressure, mass of reforming catalyst, air flow rate and operating Steam-to-Carbon ratio (STCR) ($STCR \triangleq k\dot{N}_o\mathcal{X}_{5,a}/[\dot{N}_f + k\dot{N}_o\mathcal{X}_{1,a} + k\dot{N}_o\mathcal{X}_{2,a}]$, [34]). Thus, Eq.(7) represents *an invariant relationship* between steady-state fuel utilization U_{ss}, fuel cell current i_{fc}, and fuel flow rate $\dot{N}_f$. Given a target U_{ss}, it can be used to determine $\dot{N}_f$ if i_{fc} is known and vice-versa. The invariance is attributed to the definition of U in Eq.(3), which is based on maximum hydrogen producing ability of the internal reforming reactions.

Consider the demanded fuel cell current to be $i_{fc,d}$. Then from Eq.(7), the corresponding fuel demand $\dot{N}_{f,d}$ that satisfies a target U_{ss} is

$$\dot{N}_{f,d} = \frac{i_{fc,d}\mathcal{N}_{cell}}{4nFU_{ss}}\left[1 - (1 - U_{ss})\,k\right] \tag{8}$$

Eq.(8) only addresses steady-state behavior. Hence we must assess its effectiveness in the

presence of transient current demand. Control of U using Eq.(8) is shown through sample simulations in Fig.2. The SOFC system model, with cell length of 50cm and cell area of

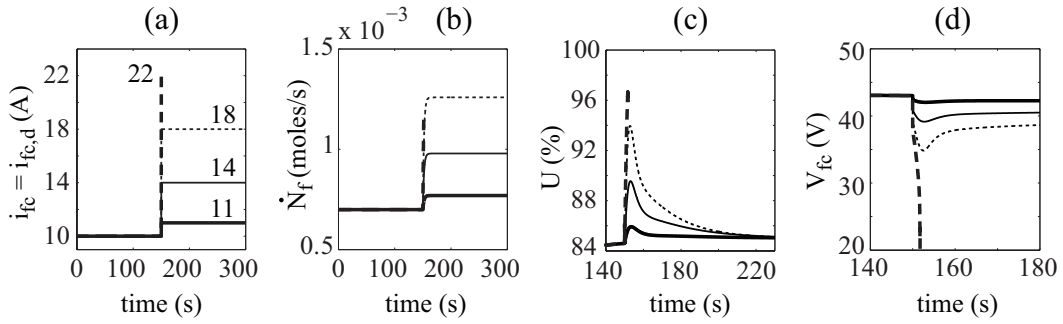

Figure 2: Open-Loop Control of U Using Eq.(8)

251cm^2, is simulated with $\mathcal{N}_{cell} = 50$ and with $i_{fc} = 10$A for $t < 150$s and target $U_{ss} = 85\%$. As mentioned in the Introduction, such high fuel utilization is desirable from the cell's electric efficiency standpoint. Four simulations are presented with $i_{fc} = 11, 14, 18, 22$A for $t \geq 150$s, Fig.2(a). The actual fuel injected, $\dot{N}_f$, is shown in Fig.2(b). Note that while $\dot{N}_{f,d}$ changes instantaneously according to Eq.(8), $\dot{N}_f$ experiences a lag. This is due to the lag introduced by the fuel supply system consisting of fuel pump and/or valves, to be discussed further in sections 4 and 5. At steady-state, $\dot{N}_f = \dot{N}_{f,d}$. In this simulation, we have assumed a first order dynamics with a time-constant of 2s. However, similar response is obtained with other fuel supply dynamics, such as ramped or rate-limited behavior. In Fig.2(c), the plots confirm $U_{ss} = 85\%$. The results show high sensitivity of transient U to load fluctuations in open-loop operation. V_{fc} is plotted in Fig.2(d). The simulation abruptly ended when the step increase was > 10A. This is due to hydrogen starvation, manifested by $U \rightarrow 100\%$ and $V_{fc} \rightarrow 0$, as seen in Figs.2(c) and (d).

From Fig.2 we make the following observations. Under open-loop control, the SOFC is capable of handling limited amount of current fluctuation with U deviating from target U_{ss} during transients. This deviation is a result of the time delay between a change in the fuel command $\dot{N}_{f,d}$ and its corresponding effect in the fuel cell. Also, V_{fc} experiences overshoot or undershoot during transient.

4 CURRENT REGULATION

The advantage of the approach in section 3 is that target U_{ss} is achieved without the knowledge of internal flow rates, temperatures, species concentrations or reaction rates. However, it leads to transient deviations in U. We address this issue by dynamically shaping i_{fc} using feedback. Noting that $\dot{N}_f \neq \dot{N}_{f,d}$ during transients, the fuel cell current i_{fc} is shaped using Eq.(7), as follows:

$$i_{fc} = \frac{4nFU_{ss}\dot{N}_f}{\mathcal{N}_{cell}} \frac{1}{[1-(1-U_{ss})\,k]} \tag{9}$$

Implementing Eq.(9) requires the measurement of the actual fuel flow $\dot{N}_f$, which is assumed to be available. The feedback based current regulation scheme and the open loop approach are shown in Fig.3 by the switch positions CR and OL respectively. Note that $\dot{N}_f$ is measured upstream of the reformer where the flow consists of pure methane. The reformed flow downstream of the reformer consists of a mixture of CH_4, CO, CO_2, H_2 and H_2O, whose composition and flow rate are assumed to be unknown. The proposed method has similarities

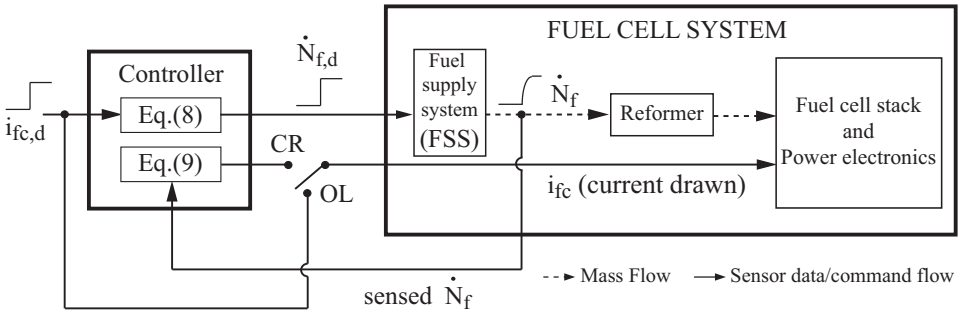

Figure 3: Scheme for Transient Utilization Control

with existing model-based load governors proposed in [9, 38] for PEMFC and SOFC-GT systems. Another related approach appears in [39] where a filter is added to the fuel cell power request based on the characteristics of the air delivery system. In comparison, using the sensed fuel in conjunction with the invariant relationship in Eq.(9) obviates the need for characterization of the fuel supply system (FSS), Fig.3. Although considered feedback based regulation, note that with respect to the fuel cell stack and power electronics subsystem of Fig.3, the proposed method of regulating i_{fc} would be a scheduled feed-forward.

Simulations are presented in Fig.4 to demonstrate the effect of current regulation on transient utilization and voltage. The system simulated is the same as that in Fig.2. Referring

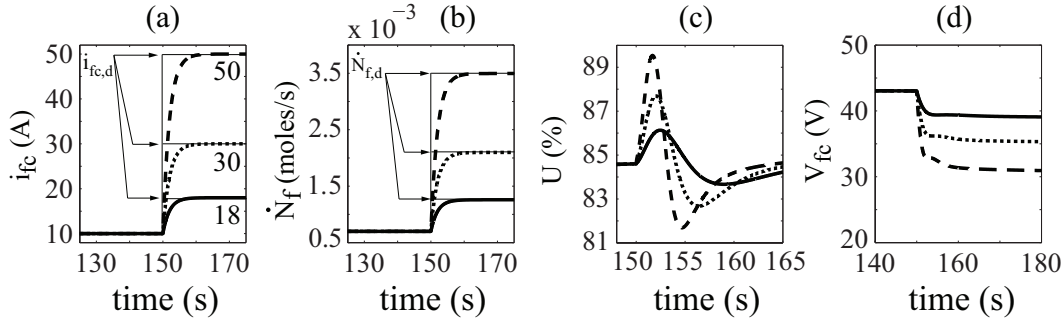

Figure 4: Effect of i_{fc} Regulation on Transient U and V_{fc}

to Fig.3, the simulation results represent the current regulation (CR) mode. Three simulations are presented, with target $U_{ss} = 85\%$, $i_{fc} = 10$A for $t < 150$s, and $i_{fc,d} = 18, 30, 50$A for $t \geq 150$s. In response to the step changes in $i_{fc,d}$, the target fuel $\dot{N}_{f,d}$ also undergoes step changes, Figs.4(a) and (b). $\dot{N}_f$ changes according to the fuel supply dynamics which is assumed to be first order with a time constant of 2s, Fig.4(b). Measured $\dot{N}_f$ is assumed to be available and the shaped i_{fc} is computed using Eq.(9) and is shown in Fig.4(a). The resulting transient U and V_{fc} are shown in Figs.4(c) and (d).

It is evident from the results above that regulation of i_{fc} drastically reduces transient U and attenuates overshoot and undershoot in V_{fc}. For instance, the step change to $i_{fc,d} = 18$A led to a deviation in U up to $\approx 94\%$ in the open-loop mode (Fig.2(c)), and only $\approx 86\%$ in closed-loop mode (Fig.4(c)). Current regulation also increases the fuel cell's transient current handling capability considerably. Even with a step change to $i_{fc,d} = 50$A, transient U remains within a $\pm 5\%$ range. We next discuss the physical reasons for transient deviation in U.

5 DELAYS INDUCED ALONG FUEL PATH

At the end of section 3, we observed that the transient deviation of U from target U_{ss} is due to delays induced along the fuel path. We attribute the delays to two primary factors,

D1: The lag between $\dot{N}_{f,d}$ and $\dot{N}_f$ introduced by the fuel supply system (FSS), and

D2: The dynamics of fuel processor (reformer) and anode.

Current regulation in section 4 compensates for D1. The residual transient in U shown in Fig.4(c) is attributed to D2. In sections 3 and 4 we assumed a first order dynamics of the FSS. However, the observations made above are applicable to a wide variety of dynamic responses. As an example, we consider a ramped response of the FSS in Fig.5. For $t < 150$s,

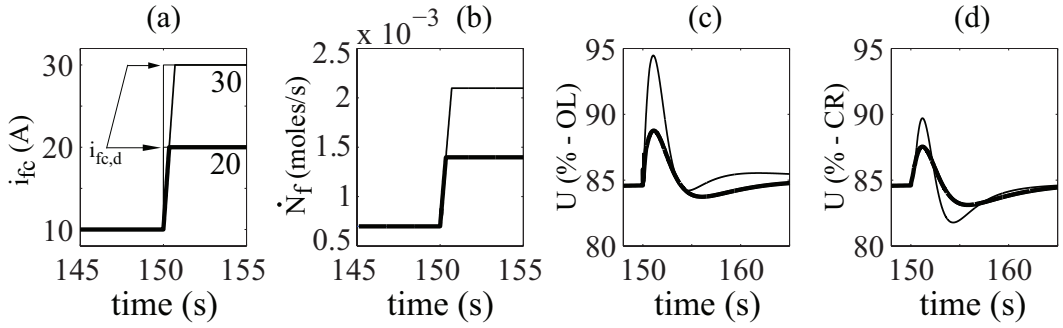

Figure 5: Open Loop and Current Regulated Responses for Ramped $\dot{N}_f$

$i_{fc} = 10$A. Two simulations are shown, with $i_{fc,d} = 20$ and 30A for $t \geq 150$s. $\dot{N}_f$ ramps at a rate of 0.002moles/s in response to change in $i_{fc,d}$, Fig.5(b). As shown in Fig.5(a), $i_{fc} = i_{fc,d}$ in OL and is ramped in CR. U in OL and CR configurations are shown in Figs.5(c) and (d) respectively. As before, we observe significant deviation in U in OL mode that is considerably attenuated in CR mode.

As the delay D1 becomes smaller, the effect of current regulation diminishes. This trend is shown in Fig.6 where for $t < 150$s, $i_{fc} = 10$A and $i_{fc,d} = 15$A for $t \geq 150$s. Three simulations are shown, all with first order fuel-supply dynamics and time-constants chosen as 0.5s, 2s and 6s. It is clear from Fig.6 that greater the delay D1, greater is the degradation of the transient response of U in OL mode, and greater is the effect of current regulation. For perfect disturbance rejection, i_{fc} must be further regulated to compensate for delay D2. The effect D1 is more pronounced than D2 in majority of cases. However, the effect of D2 is magnified when the reformer's void volume is much larger compared to the anode volume or when there exists severe flow restriction between the reformer and the anode. The latter effect is demonstrated in Fig.7, where the corresponding friction factor is increased by a

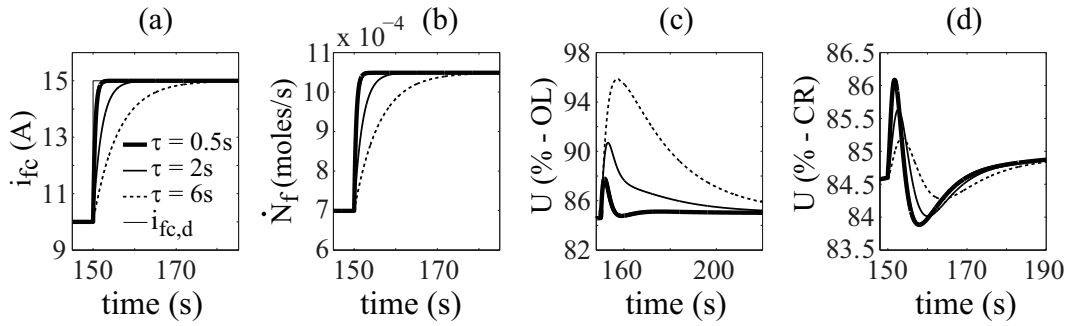

Figure 6: Effect of D1 on Transient U in OL and CR Modes

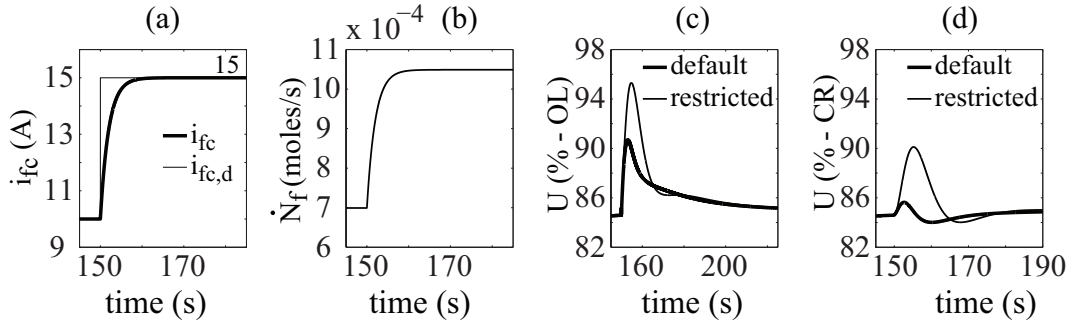

Figure 7: Effect of D2 on Transient U in OL and CR Modes

factor of 100 in the model. In the presence of heightened flow restriction, the transient deviation in U is not as well attenuated as in the default case.

6 HYBRID FUEL CELL CONFIGURATION

Regulation of i_{fc} leads to a mismatch between the demanded power and the fuel cell delivered power. This mismatch is compensated by augmenting the fuel cell with an ultra-capacitor. The hybrid system architecture used in this research is shown in Fig.8. The architecture has similarities to that adopted in [10]. Alternate approaches for interfacing fuel cell and ultra-capacitor/battery are discussed in [4, 6, 40] and references therein. In Fig.8, the fuel cell and the ultra-capacitor are connected to the electrical bus through DC/DC converters, C_1 and C_2. In the ensuing control development, we treat the DC/DC converters as static power conversion devices. From Fig.8, we have the instantaneous power balance equation

$$V_L i_L = \eta_1 V_{fc} i_{fc} + \eta_2 V_{uc} i_{uc} \tag{10}$$

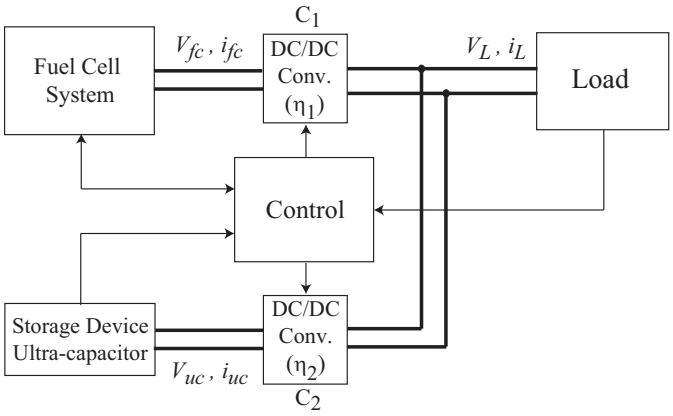

Figure 8: Hybrid Fuel Cell System

7 CONTROL DESIGN

7.1 Control Objectives

Based on the system described in section 6 the control objectives are,

- supply the net power demand $V_L i_L$ at any instant,
- attenuate fluctuation of U through current regulation, as per section 4, and
- maintain the SOC of the ultra-capacitor at a target value,

under the influence of power fluctuations and in the presence of system uncertainties. Control is designed with the following considerations:

1. The bus (supply) voltage V_L is held constant. This can be implemented by operating C_1 in voltage control mode and C_2 in the current control mode or vice-versa. Without any loss of generality, we follow the former combination with C_2 following the commanded ultra-capacitor current $i_{uc,c}$ (we treat $i_{uc} = i_{uc,c}$).
2. The ultra-capacitor current i_{uc} and the fuel demand $\dot{N}_{f,d}$ are treated as control inputs.
3. Measurements of V_{fc}, V_{uc}, i_L, i_{fc} and $\dot{N}_f$ are available.

4. The DC/DC converter efficiencies η_1 and η_2 are unknown and time varying with known upper and lower bounds. The bounds are expressed as follows

$$0 < \eta_{1,min} \leq \eta_1(t) \leq \eta_{1,max}, \quad 0 < \eta_{2,min} \leq \eta_2(t) \leq \eta_{2,max} \tag{11}$$

The controller uses the upper and lower bounds given in Eq.(11), and nominal values $\bar{\eta}_1 \in [\eta_{1,min}, \eta_{1,max}]$ and $\bar{\eta}_2 \in [\eta_{2,min}, \eta_{2,max}]$.

7.2 Nonlinear Control

We now detail a nonlinear control strategy given schematically in Fig.9. The strategy incorporates fuel cell current regulation shown in Fig.3. However in comparison, Fig.9 uses i_{uc} as a control input instead of i_{fc}. This is due to our specific hardware configuration, as mentioned in condition 1 above. $\dot{N}_{f,d}$ is the second input. Let the fuel cell serve as the primary

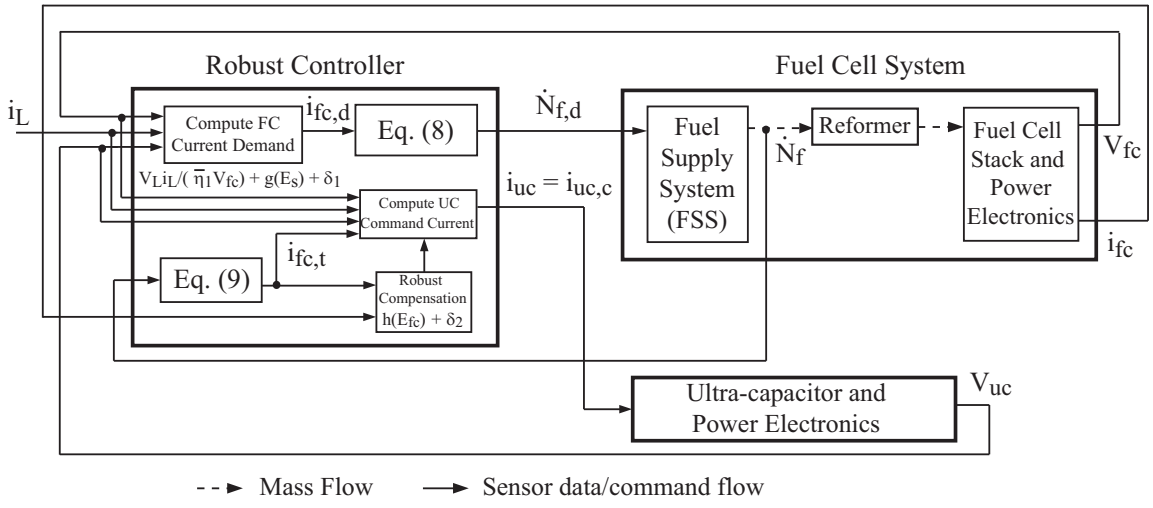

Figure 9: Nonlinear Control Approach

energy source with the ultra-capacitor supplying transient demands. Additionally, if η_1 was known, then at any instant the fuel cell current demand $i_{fc,d} = V_L i_L / \eta_1 V_{fc}$. However, for controlling the ultra-capacitor's SOC under the uncertainty in η_1, we design

$$i_{fc,d} = \frac{V_L i_L}{\bar{\eta}_1 V_{fc}} + g(E_s) + \delta_1, \quad E_s = S - S_t, \quad S = \frac{V_{uc}}{V_{max}} \tag{12}$$

where S is the instantaneous SOC of the ultra-capacitor, S_t is the target SOC, and V_{max} is the maximum ultra-capacitor voltage. The function $g(E_s)$ and the robustness term δ_1 will be designed in the ensuing analysis. The fuel demand $\dot{N}_{f,d}$, is an algebraic function of $i_{fc,d}$, given by Eq.(8), that satisfies the desired U_{ss}. The target fuel cell current $i_{fc,t}$, is based on $\dot{N}_f$ as shown in Fig.9, and is computed using Eq.(9), expressed as

$$i_{fc,t} = \frac{4nFU_{ss}\dot{N}_f}{\mathcal{N}_{cell}} \frac{1}{[1-(1-U_{ss})\,k]} \tag{13}$$

The current $i_{fc,t}$ in Eq.(13) must be achieved to obtain the steady-state utilization U_{ss}. In the presence of uncertainties, it is achieved through the ultra-capacitor current command,

$$i_{uc} = i_{uc,c} = \frac{V_L i_L - \bar{\eta}_1 V_{fc} i_{fc,t}}{\bar{\eta}_2 V_{uc}} + h\left(E_{fc}\right) + \delta_2, \quad E_{fc} = i_{fc} - i_{fc,t}, \tag{14}$$

where the function $h\left(E_{fc}\right)$ and the robustness term δ_2 will be designed in the ensuing analysis. Our control objectives are to stabilize the origin $E_s = E_{fc} = 0$ in the presence of i_L with the designs of $i_{fc,d}$ and i_{uc} in Eqs.(12) and (14) respectively. We now state the following assumptions about the fuel supply system (FSS):

- The FSS is assumed to be a combination of components such as a fuel pump and/or valves and a controller. The closed-loop system delivers flow $\dot{N}_f$ in response to $\dot{N}_{f,d}$.
- The dynamic equation of $\dot{N}_f$, $\ddot{N}_f = f\left(\dot{N}_f, \dot{N}_{f,d}, t\right)$, is assumed to be unknown.
- $\dot{N}_f$ tracks the reference signal $\dot{N}_{f,d}$ such that the error $E_{fl} = \dot{N}_f - \dot{N}_{f,d}$, satisfies a general characteristic. In Theorem 1 we assume $|E_{fl}|$ to decay exponentially, which is relaxed to boundedness of E_{fl} in Theorem 2.

We state and prove the following theorems:

Theorem 1 *If $E_{fl}(t)$ satisfies a general exponential decay condition given by*

$$|E_{fl}(t)| \leq \gamma\,|E_{fl}(t_0)|\; e^{-\zeta(t-t_0)},\; \forall\; |E_{fl}(t_0)| < r_0 \tag{15}$$

where $\gamma, \zeta, r_0 > 0$ are constants, then the hybrid SOFC system in Fig.8, with the control approach in Fig.9, satisfies exponential stability of the origin of $\mathcal{E} = [E_s \; E_{fc,t} \; E_{fc}]^T$, $E_{fc,t} = i_{fc,t} - i_{fc,d}$, with $i_{fc,d}$ and i_{uc} as in Eqs.(12) and (14) respectively,

$$g(E_s) = -k_s\, E_s, \quad k_s > 0, \qquad h(E_{fc}) = k_p E_{fc} + k_d \dot{E}_{fc}, \quad k_p, k_d > 0, \tag{16}$$

and δ_1 and δ_2 are chosen to satisfy

$$\delta_1 \begin{cases} \leq & (V_L i_L / V_{fc})\,(1/\eta_{1,max} - 1/\bar{\eta}_1) \quad for \quad E_s > 0 \\ \geq & (V_L i_L / V_{fc})\,(1/\eta_{1,min} - 1/\bar{\eta}_1) \quad for \quad E_s \leq 0 \end{cases} \tag{17}$$

$$\delta_2 \begin{cases} \geq & \beta_u \quad for\, E_{fc} > 0 \\ \leq & \beta_l \quad for\, E_{fc} \leq 0 \end{cases}, \quad \begin{array}{rcl} \beta_u & = & \frac{1}{V_{uc}} \left[V_L i_L \left(\frac{1}{\eta_{2,min}} - \frac{1}{\bar{\eta}_2} \right) - V_{fc} i_{fc} \left(\frac{\eta_{1,min}}{\eta_{2,max}} - \frac{\bar{\eta}_1}{\bar{\eta}_2} \right) \right] \\ \beta_l & = & \frac{1}{V_{uc}} \left[V_L i_L \left(\frac{1}{\eta_{2,max}} - \frac{1}{\bar{\eta}_2} \right) - V_{fc} i_{fc} \left(\frac{\eta_{1,max}}{\eta_{2,min}} - \frac{\bar{\eta}_1}{\bar{\eta}_2} \right) \right] \end{array} \tag{18}$$

Proof: From Eqs.(8), (13) and Fig.9, we have

$$\dot{N}_{f,d} = \sigma i_{fc,d},\; \dot{N}_f = \sigma i_{fc,t},\; \sigma = \frac{\mathcal{N}_{cell}}{4nFU_{ss}} \left[1 - (1 - U_{ss})\, k \right],\; \Rightarrow\; E_{fl} = \sigma E_{fc,t} \tag{19}$$

where σ is constant. Eqs.(15) and (19) imply

$$|E_{fc,t}(t)| \leq \gamma\, |E_{fc,t}(t_0)|\; e^{-\zeta(t-t_0)},\; \forall\; |E_{fc,t}(t_0)| < r_0/\sigma \tag{20}$$

We observe from Eq.(20) and *Converse Lyapunov Theorems* [17], that there exists a positive definite function $\bar{V}_{fc}$ and constants α_1, α_2, α_3, such that,

$$\alpha_1 E_{fc,t}^2 \leq \bar{V}_{fc}(E_{fc,t}, t) \leq \alpha_2 E_{fc,t}^2, \quad 0 < \alpha_1 < \alpha_2 \quad \text{and} \quad \dot{\bar{V}}_{fc} \leq -\alpha_3 E_{fc,t}^2, \quad \alpha_3 > 0 \tag{21}$$

We choose the Lyapunov function candidate $\bar{V} = 0.5\left(E_s^2 + E_{fc}^2\right) + \bar{V}_{fc}$ and note that it is positive definite and decrescent with

$$\min(\alpha_1, 0.5)\|\mathcal{E}\|^2 \leq \bar{V} = \frac{1}{2}\left(E_s^2 + E_{fc}^2\right) + \bar{V}_{fc} \leq \max(\alpha_2, 0.5)\|\mathcal{E}\|^2,\ \mathcal{E} = [E_s\ E_{fc,t}\ E_{fc}]^T \quad (22)$$

Next, from the dynamical equation of the ultra-capacitor and using Eq.(12) we have,

$$\dot{V}_{uc} = -i_{uc}/C\ \Rightarrow\ \dot{E}_s = -i_{uc}/(CV_{max}) \quad (23)$$

From Eqs.(10), (12), (14), (16) and (23), noting that

$$E_{fc} = i_{fc} - i_{fc,t},\ E_{fc,t} = i_{fc,t} - i_{fc,d}\ \Rightarrow\ i_{fc} = E_{fc} + E_{fc,t} + i_{fc,d}$$

we have,

$$\dot{E}_s = -\left(1/CV_{max}\right)\left[\left(V_L i_L/\eta_2 V_{uc}\right) - \left(\eta_1 V_{fc}/\eta_2 V_{uc}\right)\left\{E_{fc} + E_{fc,t} + \left(V_L i_L/\bar{\eta}_1 V_{fc}\right) - k_s E_s + \delta_1\right\}\right] \quad (24)$$

Next, note from Eqs.(10), (14) and (16) that

$$V_L i_L = \eta_1 V_{fc} i_{fc} + \eta_2 V_{uc}\left[\frac{V_L i_L - \bar{\eta}_1 V_{fc} i_{fc,t}}{\bar{\eta}_2 V_{uc}} + k_p E_{fc} + k_d \dot{E}_{fc} + \delta_2\right] \quad (25)$$

Rearranging Eq.(25) we have

$$\dot{E}_{fc} = -\alpha E_{fc} + \frac{\beta - \delta_2}{k_d} \quad (26)$$

where,

$$\alpha = \left[k_p/k_d + \left(V_{fc}/k_d V_{uc}\right)\left(\bar{\eta}_1/\bar{\eta}_2\right)\right] > 0, \quad \beta = \frac{1}{V_{uc}}\left[V_L i_L\left(\frac{1}{\eta_2} - \frac{1}{\bar{\eta}_2}\right) - V_{fc} i_{fc}\left(\frac{\eta_1}{\eta_2} - \frac{\bar{\eta}_1}{\bar{\eta}_2}\right)\right] \quad (27)$$

From Eqs.(21), (22), (24) and (26), we have,

$$\dot{\bar{V}} \leq -\mathcal{E}^T Q \mathcal{E} + \frac{E_s \eta_1 V_{fc}}{C V_{max} \eta_2 V_{uc}} \left[\delta_1 - \frac{V_L i_L}{V_{fc}} \left(\frac{1}{\eta_1} - \frac{1}{\bar{\eta}_1} \right) \right] + \frac{E_{fc}}{k_d} (\beta - \delta_2) \tag{28}$$

$$\mathcal{E} = \begin{bmatrix} E_s \\ E_{fc,t} \\ E_{fc} \end{bmatrix}, \quad Q = m \begin{bmatrix} k_s & -0.5 & -0.5 \\ -0.5 & \alpha_3/m & 0 \\ -0.5 & 0 & \alpha/m \end{bmatrix}, \quad m = \frac{\eta_1 V_{fc}}{C V_{max} \eta_2 V_{uc}} \tag{29}$$

Note in Eq.(29) that Q is symmetric. Furthermore, $m > 0$ and has finite positive upper and lower bounds over the range of operation of the hybrid system. Note that α_3 is not a tunable parameter since it is determined by the dynamics of the FSS. However, by choosing k_s and α appropriately, we can ensure $Q > 0 \; \forall \; m$. Thus, from the *Rayleigh-Ritz Inequality* [41]

$$\mathcal{E}^T Q \mathcal{E} \geq \inf \left(\lambda_{min,Q} \right) ||\mathcal{E}||^2 > 0 \quad \forall \; \mathcal{E} \neq 0 \tag{30}$$

where $\lambda_{min,Q}$ represents the smallest eigenvalue of Q at any instant. Furthermore, by choosing δ_1 and δ_2 to satisfy Eqs.(17) and (18), we have from Eqs.(28) and (30)

$$\dot{\bar{V}} \leq -\mathcal{E}^T Q \mathcal{E} \leq - \inf \left(\lambda_{min,Q} \right) ||\mathcal{E}||^2 < 0, \quad \forall \; \mathcal{E} \neq 0 \tag{31}$$

The conditions in Eqs.(17) and (18) are implementable with the available voltage and current measurements and known upper and lower bounds of η_1 and η_2. From Eqs.(21), (22) and (31), we conclude that the control design in Eqs.(12) and (14), with functions $g(E_s)$, $h(E_{fc})$ designed as in Eq.(16), and δ_1, δ_2 chosen as in Eqs.(17) and (18) respectively, guarantee exponential stability of $\mathcal{E} = 0$. This completes the proof (see Theorem 4.10 of [17]). $\diamond\diamond\diamond$

Theorem 2 *If E_{fl} is bounded, then the system in Eqs.(24) and (26) with state vector $\bar{\mathcal{E}} = [E_s \; E_{fc}]^T$, input $E_{fc,t}$, and δ_1 and δ_2 designed as in Eqs.(17) and (18) respectively, is Input-to-State Stable, ISS [17].*

Proof: From Eq.(19), boundedness of E_{fl} implies boundedness of $E_{fc,t}$. Choosing the following positive definite and decrescent Lyapunov function candidate

$$\bar{V} = \left(E_s^2 + E_{fc}^2\right)/2 \tag{32}$$

we have

$$\begin{aligned}
\dot{\bar{V}} &\leq -\bar{\mathcal{E}}^T \bar{Q} \bar{\mathcal{E}} + \tfrac{E_s \eta_1 V_{fc}}{C V_{max} \eta_2 V_{uc}} \left[(\delta_1 + E_{fc,t}) - \tfrac{V_L i_L}{V_{fc}} \left(\tfrac{1}{\eta_1} - \tfrac{1}{\bar{\eta}_1} \right) \right] + \tfrac{E_{fc}}{k_d} (\beta - \delta_2) \\
\bar{Q} &= m \begin{bmatrix} k_s & -0.5 \\ -0.5 & \alpha/m \end{bmatrix}, \quad m = \eta_1 V_{fc}/(C V_{max} \eta_2 V_{uc}) > 0
\end{aligned} \tag{33}$$

where α and β are defined in Eq.(27). By choosing k_s and α appropriately, we can ensure $\bar{Q} > 0$ for all feasible m. Furthermore, by choosing δ_1 and δ_2 to satisfy Eqs.(17) and (18) respectively, we have from Eq.(33),

$$\begin{aligned}
\dot{\bar{V}} &\leq -\bar{\mathcal{E}}^T \bar{Q} \bar{\mathcal{E}} + (\eta_1 V_{fc}/C V_{max} \eta_2 V_{uc}) E_s E_{fc,t} \\
&\leq -\inf\left(\lambda_{min,\bar{Q}}\right) ||\bar{\mathcal{E}}||^2 + (\eta_1 V_{fc}/C V_{max} \eta_2 V_{uc}) ||\bar{\mathcal{E}}|| \, |E_{fc,t}(t)| \\
&\leq -\inf\left(\lambda_{min,\bar{Q}}\right) (1-\theta) ||\bar{\mathcal{E}}||^2, \quad 0 < \theta < 1 \\
&< 0, \quad \forall \quad ||\bar{\mathcal{E}}|| \geq \eta_1 V_{fc} / \left[C V_{max} \eta_2 V_{uc} \, \theta \, \inf\left(\lambda_{min,\bar{Q}}\right) \right] |E_{fc,t}(t)|
\end{aligned} \tag{34}$$

The conditions of Theorem 4.19 of [17] are satisfied and we conclude the system is ISS. $\diamond\diamond\diamond$

The system in Eqs.(24) and (26) is obtained with $i_{fc,d}$ and i_{uc} as in Eqs.(12) and (14), and functions $g(E_s)$ and $h(E_{fc})$ designed as in Eq.(16). The bound on $\bar{\mathcal{E}}$ will depend on the bound on $E_{fc,t}$. Hence, the more accurately $\dot{N}_f$ tracks $\dot{N}_{f,d}$, lower will be the bound on $\bar{\mathcal{E}}$. The boundedness condition of Theorem 2 is less restrictive and more realistic than exponential decay considered in Theorem 1.

7.3 H_∞ Control

The nonlinear control discussed in section 7.2 leads to a custom algorithm that addresses system uncertainties. We also explore the application of standard robust control techniques for this problem. The advantage of standard methods lies in the availability of computational tools for controller synthesis. Specifically, we show that the simplicity of the ultra-capacitor's dynamic model, Eq.(23), allows the design of an H_∞ control for SOC regulation. Referring to Fig.9 and Eq.(12), the only difference introduced by the H_∞ approach compared to the nonlinear control in section 7.2 is that $i_{fc,d}$ is computed as

$$i_{fc,d} = V_L i_L / \bar{\eta}_1 V_{fc} + \delta_{i_{fc}} \tag{35}$$

where, $\delta_{i_{fc}}$ is obtained through an H_∞ synthesis. From Eqs.(10) and (23), we have

$$\dot{V}_{uc} = [V_L i_L - \eta_1 V_{fc} i_{fc}]/CV_{uc}\eta_2 \tag{36}$$

Expressing i_{fc} as $i_{fc} = i_{fc,d} + \epsilon$, where ϵ represents a bounded unknown error term, we get from Eqs.(35) and (36)

$$\dot{V}_{uc} = f - p(\delta_{i_{fc}} + \epsilon), \quad f = V_L i_L \left(1 - \frac{\eta_1}{\bar{\eta}_1}\right)/CV_{uc}\eta_2, \quad p = V_{fc}\eta_1/CV_{uc}\eta_2 \tag{37}$$

We design $\delta_{i_{fc}}$ as follows,

$$\delta_{i_{fc}} = \frac{1}{\hat{p}}\left(\hat{f} - v\right) \quad \Rightarrow \quad i_{fc,d} = \frac{V_L i_L}{\bar{\eta}_1 V_{fc}} + \frac{1}{\hat{p}}\left(\hat{f} - v\right) \tag{38}$$

where $\hat{f}$ and $\hat{p}$ are the estimates of the functions f and p respectively, evaluated with nominal values. Substituting for $\delta_{i_{fc}}$ from Eq.(38) into Eq.(37), we get

$$\dot{V}_{uc} = \frac{p}{\hat{p}}v + \left[f - \frac{p}{\hat{p}}\hat{f} - p\epsilon\right] \tag{39}$$

Representing $p/\hat{p}$ as a nominal value β_0 plus deviation $\Delta\beta_0$, and assigning the remaining term on the right hand side of Eq.(39) as disturbance d, we have

$$\dot{V}_{uc} = (\beta_0 + \Delta\beta)v + d \tag{40}$$

where, the modified control input v is computed using the dynamic feedback law

$$v(s) = -K_\infty(s)\, e(s), \quad e(t) = V_{uc,t} - V_{uc} \tag{41}$$

where K_∞ is controller transfer function obtained using standard H_∞ synthesis [42], and $V_{uc,t} = S_t V_{max}$ is the target ultra-capacitor voltage. The H_∞ synthesis is carried out using MATLAB®'s robust control toolbox. We end this section with the following remark:

Remark 1 *Throughout our control design, we assumed C_1 and C_2 to operate in voltage and current control modes respectively. If the combination is reversed, $E_{fc} = 0$, i.e. $i_{fc} = i_{fc,t}$, and current control of the ultra-capacitor, and hence Eq.(14), are irrelevant. Referring to Theorems 1 and 2, exponential decay of $|E_{fl}|$ and boundedness of E_{fl} would still imply exponentially stable and ISS property of $\mathcal{E} = 0$ and $\bar{\mathcal{E}}$ respectively with $i_{fc,d}$, E_s and δ_1 designed as in Eqs.(12), (16) and (17). The H_∞ control design would remain unchanged.*

The proof of the above remark is omitted for brevity. Finally, note that although stack temperature control is important, it is not considered in our control development. This is because stack temperature transients are considerably slower (order of tens of minutes) compared to transient U (order of tens of seconds) [34], [7]. Also, in absence of coolants, SOFC stack temperature is typically controlled separately by manipulating the cathode air.

8 EXPERIMENTAL TEST-STAND

We next test the control strategies developed in sections 7.2 and 7.3 on an experimental test-stand, shown in Fig.10 which implements the hybrid system schematically depicted in

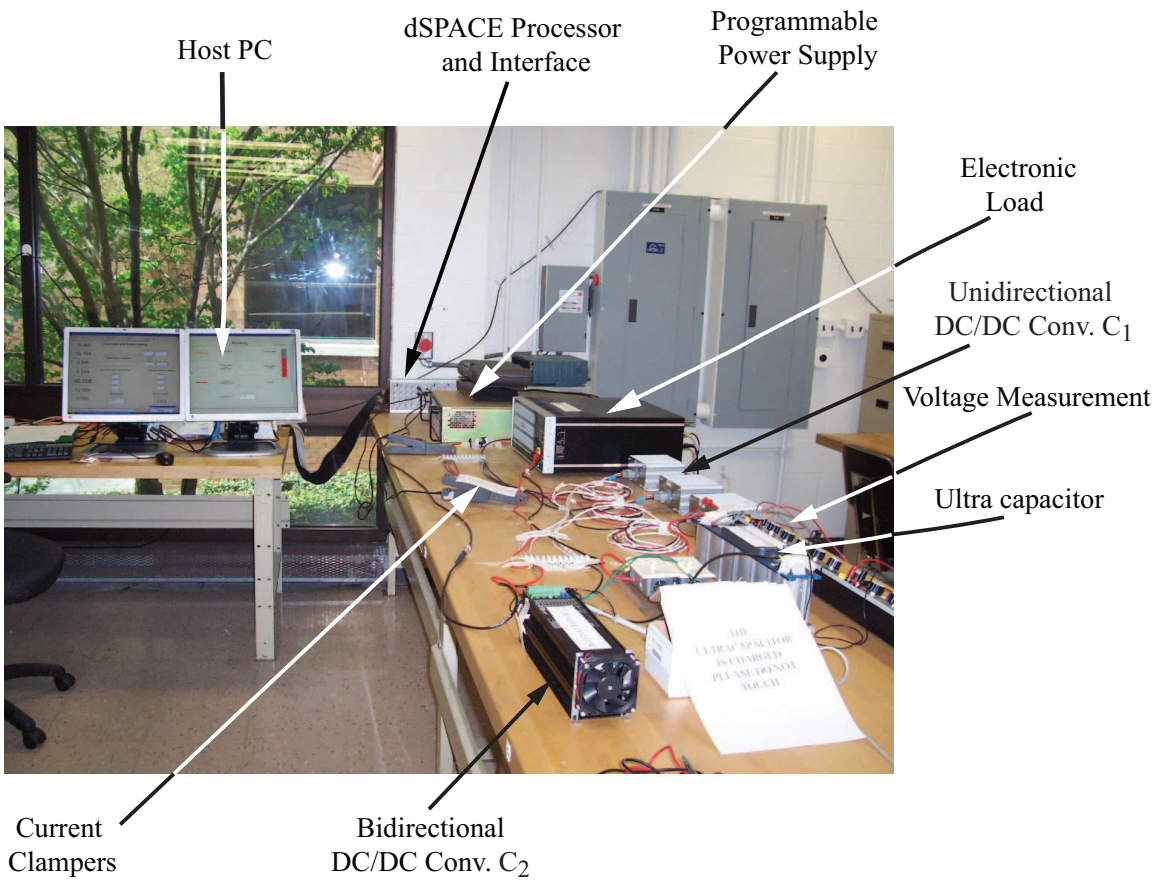

Figure 10: Experimental Test Stand

Fig.8. The test-stand consists of the following:

- *Fuel Cell Emulator:* An SOFC system is emulated by executing its mathematical model on a dSPACE® DS1103 real time processor in conjunction with a $100V/50A$ programmable power supply. A schematic diagram of the emulator is shown in Fig.11. The DS1103PPC controller is fully programmable from the MATLAB®/Simulink® environment. The power supply is run in voltage control mode with isolated analog input from the DS1103PPC controller.
- *Electronic Load:* A DC electronic load, shown in Fig.10, is used for power consumption. The electronic load can draw a maximum power of 1.8kW with a maximum voltage of 60V and a maximum current of 120A.
- *Unidirectional DC/DC Converter:* A unidirectional DC/DC converter, denoted by C_1 in Fig 11, maintains $V_L = 24$V at the output, with output current rating of ≈ 33A.

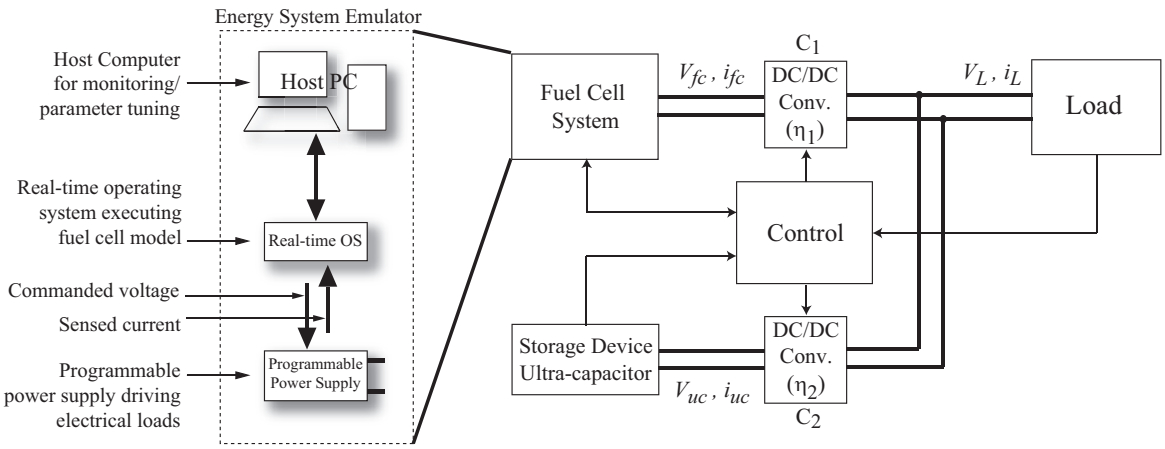

Figure 11: Fuel Cell Emulator within Hybrid Energy System

The efficiency of the converter varies between 85% and 93%.

- *Voltage Measurement:* The voltage of the ultra capacitor is measured using voltage probes with high input impedance, as shown in Fig.10.
- *The Ultra-capacitor Module:* A 16V series BMOD0250-E016 ultra capacitor from MAXWELL Technologies is used in this experimental setup. The module has specifications of $C = 250$F, $V_{max} = 16.2$V, and an internal resistance of ≈ 4.1mΩ.
- *Bidirectional DC/DC Converter:* A bidirectional DC/DC converter, denoted by C_2 in Fig.11, is used to command the ultra-capacitor current i_{uc} through analog input.
- *Current Clampers:* Current measurement is obtained using two Fluke 80i-110s AC/DC current probes, used for measuring i_L and i_{fc}.

9 EXPERIMENTAL RESULTS

In this section, we present results of experiments carried out on the test-stand described in section 8. We first present the results of the nonlinear control strategy followed by those of the H_∞ approach. In all tests, we emulate an SOFC system with 50 cells connected in series. In the plant model, the fuel supply dynamics is modeled to follow a first order dynamics with $\dot{N}_f(s) = [1/(2s+1)]\,\dot{N}_{f,d}(s)$. Neither control designs assume a knowledge of this dynamics. The bus voltage is maintained at $V_L = 24$V by converter C_1 in all experiments.

9.1 Nonlinear Control

We present results of two experiments where the nonlinear control strategy of section 9 was applied. The results are presented in Figs.12 and 13. Both experiments use the following parameter values: $U_{ss} = 0.8$, $S_t = 0.8$, $\bar{\eta}_1 = 1$, $\bar{\eta}_2 = 0.98$, $k_s = 0.1$ and $k_p = 0.2$. The parameters δ_1 and δ_2 were chosen based on Eqs.(17) and (18), as follows:

$$\delta_1 \begin{cases} = 0 & \text{for} \quad E_s > 0 \\ = \bar{\delta}_1 & \text{for} \quad E_s \leq 0 \end{cases}, \quad \delta_2 \begin{cases} = 2 & \text{for} \quad E_{fc} > 0 \\ = -2 & \text{for} \quad E_{fc} \leq 0 \end{cases} \tag{42}$$

In Fig.12, i_L follows the current profile of Fig.12(a). This profile represents a standard drive cycle obtained from [43], where the velocity variation was simply interpreted as current variation. For this test we set $\bar{\delta}_1 = 4$ and $k_d = 0.0004$. The variables related to the fuel cell, i_{fc}, V_{fc}, U and $\dot{N}_f$ are plotted in Figs.12(b), (c), (d) and (e) respectively. The results show

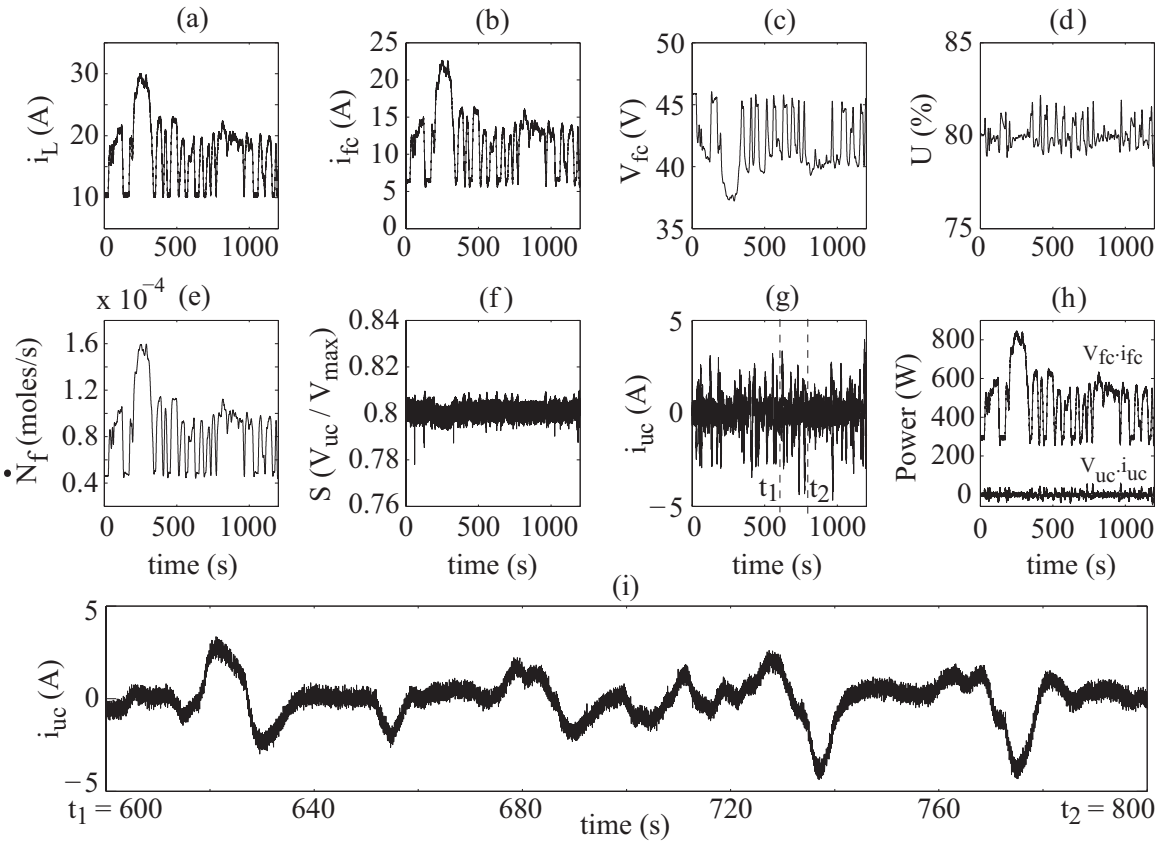

Figure 12: Nonlinear Control under Drive-cycle Variation of i_L

very close control of U in spite of rapidly varying i_L. The variables S and i_{uc} are plotted in Figs.12(f) and (g) respectively. The plots show tight control of S around the target $S_t = 0.8$. Fuel cell current i_{fc} is consistently lower than i_L since V_{fc} is higher than the bus voltage $V_L = 24$V. The rapid variation of i_{uc} around zero shows that the ultra-capacitor supplies transient power only. The ultra-capacitor current i_{uc} is magnified for $600 \leq t \leq 800$ to show its variation in detail. The fuel cell and ultra-capacitor powers are plotted in Fig.12(h).

In Fig.13(a), i_L is subject to step changes. For this test we set $\bar{\delta}_1 = 2$ and $k_d = 0.004$. The corresponding variations in i_{fc}, V_{fc}, U and $\dot{N}_f$ are plotted in Figs.13(b), (c), (d) and (e) respectively. In Fig.13(b), both i_{fc} and $i_{fc,t}$ are plotted together but the difference is not clear as they are almost coincident. S and i_{uc} are plotted in Figs.13(f) and (g) respectively,

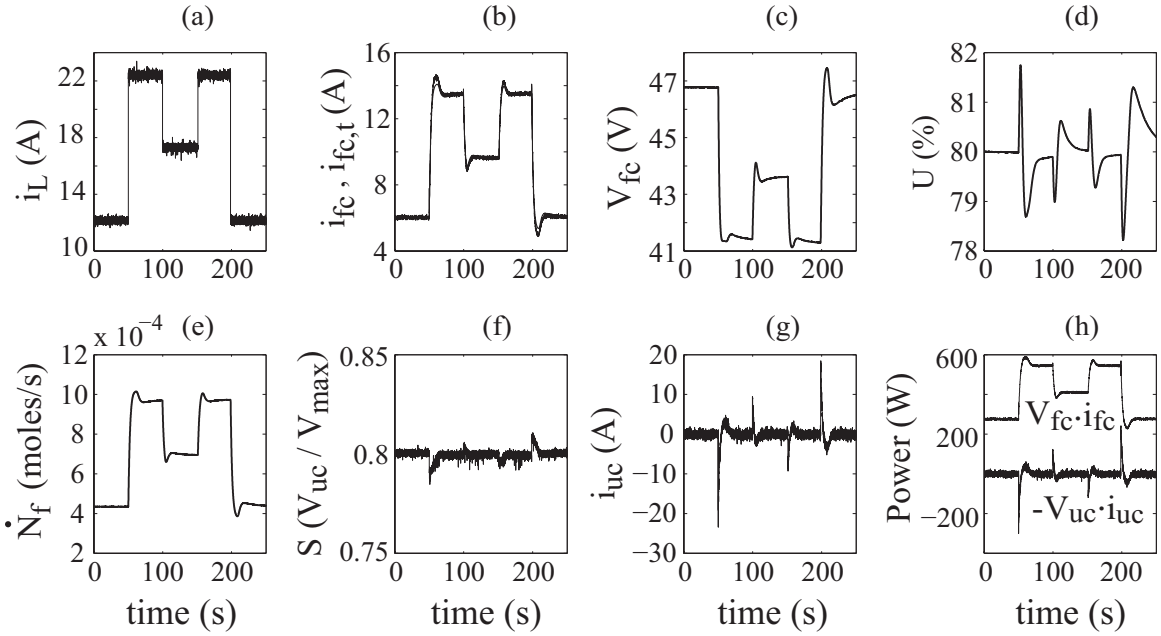

Figure 13: Nonlinear Control under Step Changes in i_L

and the fuel cell and ultra-capacitor power are plotted in Fig.13(h). The results show very close control of U in spite of drastic transients in i_L. In comparison to Figs.12(f), (g) and (h), Figs.13(f), (g) and (h), show greater variations in S, i_{uc} and the ultra-capacitor instantaneous power. This is because step changes introduce faster transients than the drive cycle.

9.2 H_∞ Control

The results of H_∞ control are presented in Fig.14. In this experiment, the following control parameters were chosen: $U_{ss} = 0.8$, $S_t = 0.8$, $k_p = 0.2$, and $k_d = 0.004$. The following ranges were chosen for uncertain quantities with nominal values at the middle of their respective ranges, $\bar{\eta}_1, \bar{\eta}_2 \in [0.8\ 1]$, $V_{fc} \in [40\ 60]$V and $V_{uc} \in [9.6\ 16.2]$V. Referring to Eq.(41), the following dynamic feedback law was determined through H_∞ synthesis,

$$K_\infty = -\frac{v(s)}{e(s)} = \frac{3.587 \times 10^4 s + 1.75 \times 10^4}{s^2 + 1049s + 105.4}$$

In Fig.14, i_L is subject to the same step changes as in Fig.13. Figs.13 and 14 indicate

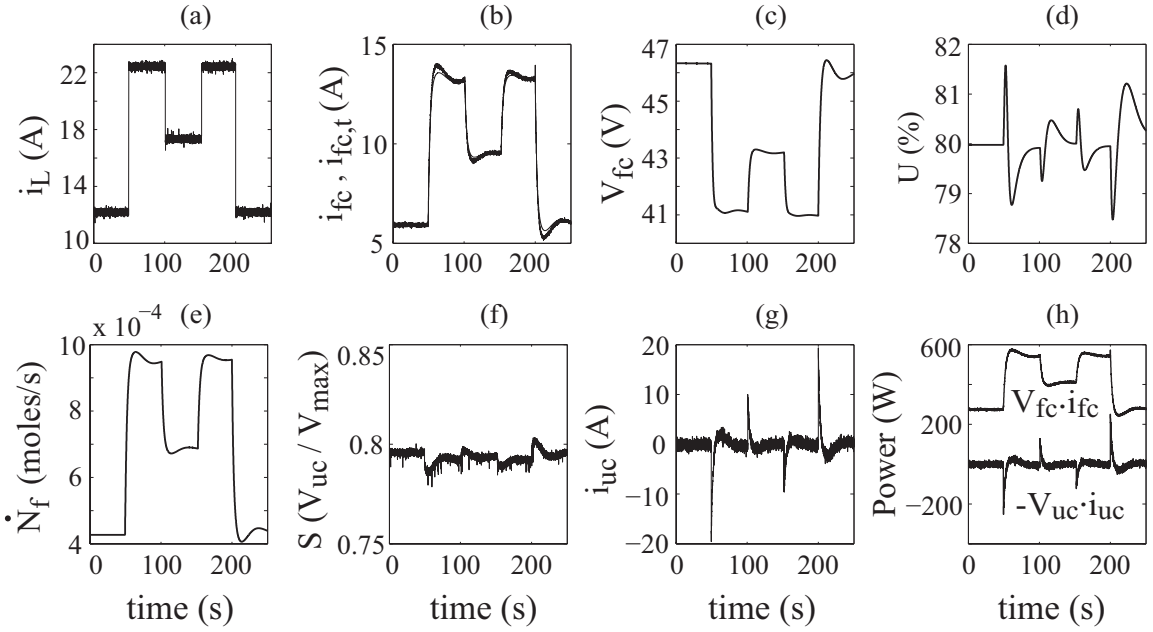

Figure 14: H_∞ Control under Step Changes in i_L

comparable performance of the H_∞ controller and the nonlinear control strategy. The only noticeable difference is in the SOC control, Figs.13(f) and 14(f), where the nonlinear control seems to perform better. While the H_∞ design was simplified due to the existence of numerical tools (MATLAB®'s robust control toolbox), it took considerable tuning effort to obtain acceptable performance. On the other hand, while controller development was more involved for the nonlinear control, tuning efforts were lesser.

10 CONCLUSION

This paper addresses the control of a hybrid SOFC ultra-capacitor system to improve its load-following capability while preventing fuel starvation in the SOFC. The fuel starvation problem is addressed through transient control of fuel utilization, U, achieved by regulating the fuel cell current i_{fc} using an invariant relationship involving U, fuel flow $\dot{N}_f$ and i_{fc}. The approach leads to a mismatch between requested power and fuel cell delivered power during transients. This mismatch is compensated by the ultra-capacitor. For the hybrid system, a comprehensive control strategy is required that incorporates current regulation and additionally controls the ultra-capacitor's SOC at a target level. To this end, two control designs are proposed. The first is a robust nonlinear control strategy for which stability properties of the closed-loop system are guaranteed. The second is a standard H_∞ approach. To test the control strategies an experimental test-stand is developed, consisting of an emulated SOFC, and actual ultra-capacitor and power-electronics components, forming a laboratory scale hybrid power system. Both control strategies show comparable performance on this platform. In future research, conditions such as saturated fuel flow, limiting current density of fuel cell, limiting ultra-capacitor current, which are more likely to occur at higher power applications, will be considered. In such cases, addition of a battery is foreseen.

11 ACKNOWLEDGMENT

The authors gratefully acknowledge the support provided by the Office of Naval Research under grant #N000140810704 in conducting this research.

References

[1] J. Larminie and A. Dicks. *Fuel Cell Systems Explained.* John Wiley & Sons, Inc., second edition, 2003.

[2] X. Li. *Principles of Fuel Cells.* Taylor and Francis Group, 2006.

[3] J. R. Meacham, F. Jabbari, J. Brouwer, J. L. Mauzey, and G. Scott Samuelsen. Analysis of stationary fuel cell dynamic ramping capabilities and ultra capacitor energy storage using high resolution demand data. *Journal of Power Sources*, 156:472–479, 2006.

[4] A. Drolia, P. Jose, and N. Mohan. An approach to connect ultracapacitor to fuel cell powered electric vehicle and emulating fuel cell electrical characteristics using switched mode converter. *Proceedings of Industrial Electronics Conference*, pages 897–901, 2003.

[5] P. Thounthong, S. Rael, and B. Davat. Control strategy of fuel cell/supercapacitors hybrid power sources for electric vehicle. *Journal of Power Sources*, 158:806–814, 2006.

[6] A. Vahidi, A. Stefanopoulou, and H. Peng. Current management in a hybrid fuel cell power system: A model-predictive control approach. *IEEE Transactions on Control Systems Technology*, 14(6):1047 – 1057, 2006.

[7] F. Mueller, J. Brouwer, F. Jabbari, and S. Samuelsen. Dynamic simulation of an integrated solid oxide fuel cell system including current-based fuel flow control. *ASME Journal of Fuel Cell Science and Technology*, 3:144–154, 2006.

[8] W. Schmittinger and A. Vahidi. A review of the main parameters influencing long-term performance and durability of PEM fuel cells. *Journal of Power Sources*, 180:1–14, 2008.

[9] J. Sun and I. Kolmanovsky. Load governor for fuel cell oxygen starvation protection: A robust nonlinear reference governor approach. *Proceeding of the 2004 American Control Conference, Boston, MA June 30 - July 2*, pages 828–833, 2004.

[10] A. Arce, A. J. del Real, and C. Bordons. MPC for battery/fuel cell hybrid vehicles including fuel cell dynamics and battery performance improvement. *Journal of Process Control*, 19:12891304, 2009.

[11] M. Uzunoglu and M. S. Alam. Dynamic modeling, design and simulation of a pem fuel cell/ultracapacitor hybrid system for vehicular applications. *Energy Conversion and Management*, 48:1544–1553, 2007.

[12] V. Paladini, T. Donateo, A. de Risi, and D. Laforgia. Super-capacitor fuel-cell hybrid electric vehicle optimization and control strategy development. *Energy Conversion and Management*, 48:3001–3008, 2007.

[13] A. Hajizadeh and M. A. Golkar. Intelligent power management strategy of hybrid distributed generation systems. *Electrical Power and Energy Systems*, 29:783–795, 2007.

[14] Z. Jiang, L. Gao, and R. A. Dougal. Adaptive control strategy for active power sharing in hybrid fuel cell/battery power sources. *IEEE Transactions on Energy Conversion*, 22(2):507–515, 2007.

[15] E. M. Fleming and I. A. Hiskens. Dynamics of a microgrid supplied by solid oxide fuel cells. *iREP Symposium - Bulk Power System Dynamics and Control - VII, Charleston, SC*, 2007.

[16] M. Y. Ayad, M. Becherif, A. Djerdir, and A. Miraoui. Sliding mode control for energy management of dc hybrid power sources using fuel cell, batteries and supercapacitors. *International Conference on Clean Electrical Power*, pages 500–505, 2007.

[17] H. Khalil. *Nonlinear Systems*. Prentice-Hall, Inc. Upper Saddle River, NJ, 3 edition, 2002.

[18] A. Payman, S. Pierfederici, and F. Meibody-Tabar. Energy control of supercapacitor/fuel cell hybrid power source. *Energy Conversion and Management*, 49:1637–1644, 2008.

[19] M. Fliess, J. Levine, P. Martin, and P. Rouchon. Flatness and defect of non-linear systems: Introductory theory and examples. *International Journal of Control*, 61(6):1327–1361, 1995.

[20] P. Rodatz, G. Paganelli, A. Sciarretta, and L. Guzzella. Optimal power management of an experimental fuel cell/supercapacitor-powered hybrid vehicle. *Control Engineering Practice*, 13:4153, 2005.

[21] A. Lazzaretto, A. Toffolo, and F. Zanon. Parameter setting for a tubular SOFC simulation model. *ASME Journal of Energy Resources Technology*, 126:40–46, 2004.

[22] K. Sedghisigarchi and A. Feliachi. Control of grid-connected fuel cell power plant for transient stability enhancement. *Proceedings of the IEEE Power Engineering Society Transmission and Distribution Conference*, 1:383–388, 2002.

[23] S. Campanari. Thermodynamic model and parametric analysis of a tubular SOFC module. *Journal of Power Sources*, 92:26–34, 2001.

[24] A. K. M. M. Murshed, B. Huang, and K. Nandakumar. Estimation and control of solid oxide fuel cell system. *Computers and Chemical Engineering*, 34:96–111, 2010.

[25] M. H. Nehrir and C. Wang. *Modeling and Control of Fuel Cells - Distributed Generation Applications*. John Wiley and Sons, Inc., Hoboken, New Jersey, 2009.

[26] R. Gaynor, F. Mueller, F. Jabbari, and J. Brouwer. On control concepts to prevent fuel starvation in solid oxide fuel cells. *Journal of Power Sources*, 180:330342, 2008.

[27] C. Stiller, B. Thorud, O. Bolland, R. Kandepu, L. Imsland, and B. A. Foss. Control strategy for a solid oxide fuel cell and gas turbine hybrid system. *Journal of Power Sources*, 158:303–315, 2006.

[28] J. T. Pukrushpan, A. G. Stefanopoulou, and H. Peng. *Control of Fuel Cell Power Systems*. Springer, 2004.

[29] H. Gorgun, M. Arcak, S. Varigonda, and S. A. Bortoff. Observer designs for fuel processing reactors in fuel cell power systems. *International Journal of Hydrogen Energy*, 30:447–457, 2005.

[30] V. Tsourapas, A. G. Stefanopoulou, and J. Sun. Model-based control of an integrated fuel cell and fuel processor with exhaust heat recirculation. *IEEE Transactions on Control Systems Technology*, 15(2):233–245, 2007.

[31] T. Das. An adaptive observer design for recirculation based solid oxide fuel cell systems using cell voltage measurement. *American Control Conference, St. Louis, MO.*, 2009.

[32] T. Das and R. Weisman. A feedback based load shaping strategy for fuel utilization control in sofc systems. *American Control Conference, St. Louis, MO.*, 2009.

[33] R. Kandepu, L. Imsland, B. A. Foss, C. Stiller, B. Thorud, and O. Bolland. Modeling and control of a SOFC-GT-based autonomous power system. *Energy*, 32:406–417, 2007.

[34] T. Das, S. Narayanan, and R. Mukherjee. Steady-state and transient analysis of a steam reformer based solid oxide fuel cell system. *ASME Journal of Fuel Cell Science and Technology*, 7(1), 2010.

[35] M. L. Ferrari, A. Traverso, L. Magistri, and A. F. Massardo. Influence of anodic recirculation transient behavior on the SOFC hybrid system performance. *Journal of Power Sources*, 149:22–32, 2005.

[36] J. Xu and G. F. Froment. Methane steam reforming, methanation and water-gas shift: I. Intrinsic kinetics. *AIChE Journal*, 35(1):88–96, 1989.

[37] R. Bove, P Lunghi, and N. M. Sammes. SOFC mathematic model for systems simulations - part 2: Definition of an analytical model. *International Journal of Hydrogen Energy*, 30:189–200, 2005.

[38] V. Tsourapas, J. Sun, and A. Stefanopoulou. Incremental step reference governor for load conditioning of hybrid fuel cell and gas turbine power plants. *IEEE Transactions on Control Systems Technology*, 17(4):756–767, 2009.

[39] Y. Guezennec, T. Choi, G. Paganelli, and G. Rizzoni. Supervisory control of fuel cell vehicles and its link to overall system efficiency and low-level control requirements. *Proceedings of the American Control Conference*, pages 2055–2061, 2003.

[40] A. G. Stefanopoulou and K. Suh. Mechatronics in fuel cell systems. *Control Engineering Practice*, 15:277289, 2007.

[41] W. J. Rugh. *Linear System Theory.* Prentice Hall, Upper Saddle River, NJ, 2 edition, 1996.

[42] S. Skogestad and I. Postlethwaite. *Multivariable Feedback Control: Analysis and Design.* John Wiley & Sons, Ltd., 2 edition, 2005.

[43] http://www.epa.gov/otaq/emisslab/testing/dynamometer.htm.